AIChE

A Multiscale, Biophysical Model of Flow-Induced Red Blood Cell Damage

Flavia Vitale
Dept. of Chemical and Biomolecular Engineering, Rice University, Houston, TX 77005

Dept. of Chemical Engineering, Materials and Environment, University of Rome "La Sapienza", Via Eudossiana 18, 00184, Rome, Italy

Jaewook Nam
Dept. of Chemical and Biomolecular Engineering, Rice University, Houston, TX 77005

School of Chemical Engineering, Sungkyunkwan University, Suwon, Korea 2066, Seobu-ro, Jangan-gu, Suwon, Gyeonggi-do 440–746, Korea

Luca Turchetti
Faculty of Engineering, Università Campus Bio-Medico di Roma, Via Àlvaro del Portillo 21, 00128, Rome, Italy

Marek Behr
Chair for Computational Analysis of Technical Systems (CATS), Center for Computational Engineering Science (CCES), RWTH Aachen University, 52056, Aachen, Germany

Robert Raphael
Dept. of Bioengineering, Rice University, Houston, TX 77005

Ken Kennedy Institute for Information Technology, Rice University, Houston, TX 77005

The Smalley Institute for Nanoscale Science and Technology, Rice University, Houston, TX 77005

Maria Cristina Annesini
Dept. of Chemical Engineering, Materials and Environment, University of Rome "La Sapienza", Via Eudossiana 18, 00184, Rome, Italy

Matteo Pasquali
Dept. of Chemical and Biomolecular Engineering, Rice University, Houston, TX 77005

Dept. of Chemistry, Dept. of Materials Science and NanoEngineering, Rice University, Houston, TX 77005

Ken Kennedy Institute for Information Technology, Rice University, Houston, TX 77005

The Smalley Institute for Nanoscale Science and Technology, Rice University, Houston, TX 77005

DOI 10.1002/aic.14318

A new model for mechanically induced red blood cell damage is presented. Incorporating biophysical insight at multiple length scales, the model couples flow-induced deformation of the cell membrane (~10 μm) to membrane permeabilization and hemoglobin transport (~100 nm). We estimate hemolysis in macroscopic (above ~1 mm) 2-D inhomogeneous blood flow by computational fluid dynamics (CFD) and compare results with literature models. Simulations predict the effects of local flow field on RBC damage, due to the combined contribution of membrane permeabilization and hemoglobin transport. The multiscale approach developed here lays a foundation for a predictive tool for the optimization of hydrodynamic and hematologic design of cardiovascular prostheses and blood purification devices. © 2014 American Institute of Chemical Engineers *AIChE J*, 60: 1509–1516, 2014

Keywords: hemolysis modeling, computational fluid dynamics (CFD), red blood cell, membrane poration

Introduction

In many intra- and extracorporeal biomedical devices, such as hemodialyzers, prosthetic heart valves and ventricular assist devices (VADs), blood is forced to flow through

---

Additional Supporting Information may be found in the online version of this article.

Correspondence concerning this article should be addressed to M. Pasquali at mp@rice.edu.

artificial ducts, where mechanical stresses can be up to two orders of magnitude higher than those acting in physiological blood flow,[1,2] increasing the risk of red blood cell (RBC) damage. These stresses can cause hemolysis, i.e., the release of hemoglobin (Hb), into plasma. In severe cases, hemolysis causes a decrement in RBC count and it may cause hemolytic anemia. Even in milder, sublytic instances, where Hb is released through temporary pores in the RBC membranes, other pathologies may arise, including reduction of RBC lifetime[3] and renal failure.[4] The design of biomedical devices must account for potential hemolysis to ensure not only efficacy, but also hemocompatibility.[5] Several experimental studies have been devoted to assessment of RBC damage[6,7]; they are typically carried out by flowing blood in mock-circulation loops in series with the perfused artificial device and measuring the amount of plasma-free hemoglobin (pfHb) at the end of the experiment. However, such experimental investigations can be slow and expensive because each design iteration requires the construction of a new device, and test results do not provide strong mechanistic links between design alteration and performance changes. Moreover, it is challenging to apply *in vitro* experimental results directly to *in vivo* situations.

Therefore, there is a need for a reliable quantitative and mechanistic model to assess device hemocompatibility. Such a model should handle the physics of hemolysis within reasonable computation time, allow for general results (i.e., not confined to specific experimental conditions), and identify potential device drawbacks in the early design phase, enabling both hydrodynamic and hemodynamic computer-assisted design of devices.

Early studies on hemolysis[8] identified shear stress and stress exposure time as the major factors in mechanical hemolysis. A class of "stress-based" models was developed based on the experimental correlation of measured pfHb concentration, shear stress (τ), and exposure time (t). The most common model is a power-law for the index of hemolysis (IH)

$$\mathrm{IH}=\frac{\Delta \mathrm{Hb_p}}{\mathrm{Hb_B}}=At^{\mathrm{a}}\tau^{\mathrm{b}} \tag{1}$$

where $\Delta\mathrm{Hb_p}=\mathrm{Hb_p}\text{-}\mathrm{Hb_p^0}$ is the increase in pfHb concentration above the physiological value, $\mathrm{Hb_p^0}$ is the total blood Hb concentration and A, a, b are empirical constants.[9,10]

However, this approach has several limitations. The correlations are based on data obtained by exposing blood to steady Couette flow, i.e., uniform and time-constant shear stress in the range 50–255 Pa, within a given exposure time (7–700 ms). Thus, these models are not predictive of general flow conditions: in a typical medical device the shear stress is not a simple scalar, is spatially inhomogeneous and time-dependent. In many practical situations, the magnitude of shear stress may exceed the range experimentally measured for the correlations. Finally, this solely empirical approach does not consider fundamental relationships among shear rate, cell shape distortion and hemoglobin release.

In contrast, a "strain-based" approach considers the flow-induced RBC deformation up to the membrane rupture limit, and relates hemolysis to the deformation. In the model proposed by Arora et al.[11] RBC deformation is tracked along pathlines to compute the equivalent scalar shear rate experienced by the cell and then the rate of hemolysis based on the extent of cell areal deformation. Chen et al.[12] proposed a damage model based on a threshold strain and compared model predictions to hemolysis data in hypodermic needles. Even though these two strain-based models[11,12] include more mechanistic information on hemolysis, they lack a description of membrane-level phenomena and do not capture the processes leading from partial damage to irreversible rupture, the so-called sublytic phase of RBC damage.

Table 1. Properties of RBCs (at 300 mOsm, 37°C)

	Value
Diameter [μm]	8
Cell thickness [μm]	2
Surface area [μm^2]	135
Volume [μm^3]	100
Membrane thickness [nm]	5–10
Shear modulus [$mN\ m^{-1}$]	$6\cdot10^{-3}$
Bending modulus [Nm]	$2\cdot10^{-19}$
Elastic compressibility modulus [$mN\ m^{-1}$]	400

From Guido and Tomaiulo[17]

Arora et al.[13] defined the following fundamental criteria for formulating models for hemolysis estimation (1) physical properties of RBCs and their variety from species to species, (2) blood flow conditions, (3) RBC behavior in general flows, (4) ease of implementation in complex flow configurations, and (5) ease of integration into computational fluid dynamics (CFD) analysis. Here we propose a sixth important criterion: the model must capture biophysical processes associated with RBC damage. In this work, we propose a novel model for RBC damage estimation in general flows based on a multiscale, biophysical (MSBP) approach, which accounts for both blood fluid dynamics and RBC membrane biophysics.

Background: Mechanical Properties of RBCs and Membrane Poration

RBCs at rest are axisymmetric, biconcave, disk-shaped bodies. The main physical and mechanical properties of human RBCs are summarized in Table 1. RBCs are compliant to shearing and bending but remarkably resistant to area stretching (Table 1). Due to the high-stretch resistance, the maximum area strain (α) that RBCs can tolerate ranges from 4%[14] to 6.4%.[15]

In flow, RBC membrane deforms in response to fluid-induced viscous forces, developing tension. At low tension, the membrane can deform without area dilation, because RBCs have 40% excess surface area with respect to a sphere enclosing the same volume.[16,17] As tension grows and area strain increases, the formation of membrane pores becomes energetically favorable. Pores relax the membrane tension and quickly reach a stable configuration—in a few μs for pores with radius up to 100 nm.[18] Further deformation and pore nucleation can occur up to the critical area strain for membrane rupture.

Temporary permeabilization of biological membranes under the action of strong flows was shown through the uptake of ~10 nm molecules,[19] and AFM observations of unbroken RBCs after shearing[20] showed altered membrane morphology accompanied by an increase in pfHb concentration.

Model Formulation

In our modeling approach flow-induced RBC damage consists of three main processes (Figure 1)

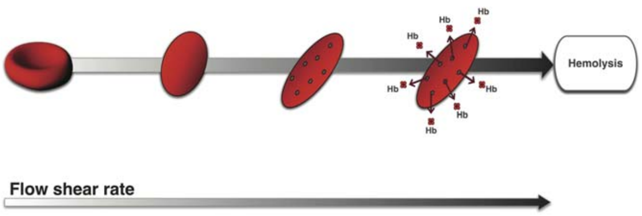

Figure 1. Framework of the MSBP model.

[Color figure can be viewed in the online issue, which is available at wileyonlinelibrary.com.]

1. Flow-induced RBC deformation and membrane area dilation.
2. Membrane energy changes and pore formation under deformation.
3. Transport of hemoglobin through pores to estimate the index of hemolysis.

Pore formation is assumed to occur instantaneously, because the relative time scale of this evolution ($\approx$10 μs)[18] is about four orders of magnitude smaller than the characteristic time scale for RBC deformation ($\approx$100 ms).[21]

The definitions and values of all the constants used in the model are reported in Table 2.

RBC deformation and area dilation in fluid flow

RBCs immersed in a flow exhibit complex motion and deformation patterns. When blood is at rest, cells aggregate in stacks called rouleaux.[22] When blood is exposed to a shear flow with low-shear rate (G_f), rouleaux disaggregate and cells tumble as naturally buoyant capsules, while preserving their biconcave shape. As the fluid shear rate increases, tumbling ceases and cells deform into ellipsoidal shapes, with the major axis leaning along the direction of flow.[23] In shear flow this occurs at a shear stress of about 1 Pa. In this regime, the membrane starts to rotate around the cytoplasm, in the so-called tank-treading motion.[24,25] Higher shear rate causes membrane dilation. In steady shear,[8] the critical area strain (6%) is reached when G_f approaches 42000 s^{-1}. Below this threshold strain, RBCs can completely recover their biconcave shape after the removal of loading.

The tensor-based model of Arora et al.[11] predicts the morphology of RBCs along their trajectories by considering stretching and contraction, membrane relaxation, rotation and tank-treading. In that work, based on the Maffettone and Minale[26] model for droplets, a symmetric, positive-definite tensor **S** is used to describe cell shape and orientation. The temporal volume-conserving cell deformation is

$$\frac{d\mathbf{S}}{dt}-[\mathbf{\Omega}\cdot\mathbf{S}-\mathbf{S}\cdot\mathbf{\Omega}]=-f_1[\mathbf{S}-g(\mathbf{S})\mathbf{I}]+f_2\left[\tilde{\mathbf{E}}\cdot\mathbf{S}+\mathbf{S}\cdot\tilde{\mathbf{E}}\right]$$
$$+f_3\left[\tilde{\mathbf{W}}\cdot\mathbf{S}-\mathbf{S}\cdot\tilde{\mathbf{W}}\right] \quad (2)$$

where $\tilde{\mathbf{E}}$ and $\tilde{\mathbf{W}}$ are, respectively the rate of strain and vorticity tensors in the frame of reference of the cell rotating with rate $\mathbf{\Omega}$ with respect to a laboratory fixed frame, and $g(\mathbf{S}) = 3\ III/II$, where III and II are the third and second invariants of **S**. Specifically, $\mathbf{\Omega}$ is the rate of rotation of the eigenvectors of **S** (see Ref.11 for details). The parameters $f_1=5s^{-1}$,$f_2=f_3=4.3\cdot 10^{-4}$, were determined by matching the model with experimental data and incorporate effects of relaxation time, long-lived shape oscillations, tank-treading and critical area strain limit.[27] The area of the ellipsoidal cell shape is computed with the method of Keller and Skalak.[28]

Membrane energy landscape under stretching and quantification of porated area

Flow-induced RBC deformation perturbs the equilibrium configuration of the membrane. Nucleation of pores is dictated by the membrane energy landscape of the perturbation. The configuration of the lipid bilayer is governed by two competing forces: hydrophobic attraction of the lipid tails and headgroup repulsion. The interfacial free energy per molecule is[29,30]

$$\mu=\sigma a_m+D/a_m, \quad (3)$$

where σ, a_m and D are the interfacial energy at the hydrocarbon-water interface, the interfacial area per molecule exposed to aqueous phase and a constant, respectively. The surface area per molecule of an undeformed membrane $a_0 = (D/\sigma)^{1/2}$, minimizes Eq. 3.

When a nonporated bilayer is stretched, it expands elastically and the total energy of the 2M lipid molecules in the membrane becomes

$$W_{IN}=2M\mu=2\sigma A_m\left(1+\frac{A_0^2}{A_m^2}\right)=2\sigma A_0\left(2+\frac{\alpha^2}{1+\alpha}\right), \quad (4)$$

where A_0 and A_m are the undeformed and total stretched area of the lipid bilayer and A_m is the area strain.

The area expansion builds up tension in the membrane, but pores can relieve the tension and minimize the total free energy. Pore formation involves two competing effects[31,32]:

1. Decrease in the total energy due to the decrease in the area subjected to the interfacial stress, which tends to expand the pore.
2. Increase in the total energy due to the exposure of hydrophobic tails to water along the pore perimeter, which tends to shrink the pore.

Both effects depend on the rigidity $\xi\geq 1$ of the hydrophobic lipid tails.[32] Considering the contribution of pores to the total free energy of the membrane yields

$$W_P=\gamma L_P+2\sigma'(A_m-A_P)\left[1+\frac{A^2{}_0}{(A_m-A_P)^2}\right], \quad (5)$$

where $\gamma=2h_{ne}\sigma'$ is the pore edge energy, h_{ne} is the nonexposed lipid tail length and $\sigma' < \sigma$ is the apparent hydrophobicity considering the stretching of lipids.[32] Pore edge energy is not constant, because h_{ne} varies with α. Following Fournier and Joos,[32] h_{ne} can be estimated by assuming that the hydrophobic surface exposed to water is represented by a cone of lateral surface $S=\xi(a-a_0)=\pi r_L h_e$, where r_L is the radius of lipids, and h_e is the length of the tails exposed to water. The nonexposed length is, therefore $h_{ne}=h_t-\xi r_L\alpha$, where h_t is the total length of lipid tails.

We consider n circular pores with radius r_p, perimeter $L_P=2\pi n r_P$ and area $A_P=\pi n r^2{}_P$. In the limit of small porated area, the normalized energy per unit area for a generic pore radius r_0 can be conveniently expressed as a fourth order polynomial[30]

$$\hat{W}_N=\hat{W}_P-\hat{W}_{IN}\approx AN^2r^4{}_0-BNr_0{}^2+CNr_0, \quad (6)$$

where $N=n/A_m$, $A=2\sigma'\xi-\sigma'_0$, $B=\sigma'_0\pi$, $C=2\pi\gamma$ and

Table 2. Values of the Model Parameters

Symbol	Value	Definition and source
Parameters reported in or estimated from literature sources		
f_1	5 s^{-1}	Relaxation parameter[11,27]
f_2, f_3	$4.3{\cdot}10^{-4}$	Steady shear deformation parameters[11,27]
A_0	135 μm^2	Unstretched area of RBCs[17]
σ	20–50 mJ m^{-2}	Interfacial energy at water-hydrocarbon interface[29]
σ'	3.2 mJ m^{-2}	Apparent hydrophobicity[32]
ξ	8	Lipid tail rigidity[32]
h_t	2.5 nm	Length of phospholipid tails[29]
r_L	$9.5\ 10^{-2}$ nm	Radius of phospholipid heads[29]
α_1	0.16%	Threshold area strain for pore formation[35]
α_2	6%	Threshold area strain for complete hemolysis[8,15]
N_1	$7.4{\cdot}10^{-3}$ μm^{-2}	Minimum pore density (model parameter)
N_2	111 μm^{-2}	Maximum pore density (model parameter)
Hct	40%	Blood hematocrit
μ	3.5 mPa s	Blood viscosity
ρ	1056 kg m^{-3}	Blood density
Parameters obtained by fitting the model to the data of Ref. 37 (Note: these parameters appear in Eq. 15).		
h	$1.67{\cdot}10^{-8}$ $\mu m\ s^{(k-1)}$	Mass transport coefficient prefactor
k	1.54	Power law dependence of mass transport coefficient on shear rate

$$\sigma_0'=\frac{\partial W_P}{\partial A_P}\bigg|_{A_P=0}=2\sigma'\xi\left[1-\frac{1}{(1+\alpha)^2}\right] \tag{7}$$

is the surface tension of the intact membrane.[30]

For $r_0>0, \hat{W}_N(r_0)$ has a local minimum, corresponding to a stable equilibrium condition. At this minimum, pores with $r_0=r_p$ form due to membrane deformation.

To close the system of equations, N must be related to the other variables. Eq. 6 requires the condition $N<N_C=8/27\,[B^3/(AC^2)]$ for any α to admit the local minimum and it yields equilibrium porated configurations. We assume that N depends on strain, because area strain drives the poration. Electroporation studies[33] showed that the equilibrium pore density on membrane pores follows a Boltzmann's type distribution. Because transmembrane voltage and area strain have similar effects on membrane poration,[34] we use the same Boltzmann-type dependence of N on area strain

$$N=N_0 exp(\zeta\alpha), \tag{8}$$

Equation 8 can be rearranged as

$$N=N_1 exp\left[\frac{\alpha-\alpha_1}{\alpha_1-\alpha_2}\ln\left(\frac{N_1}{N_2}\right)\right], \tag{9}$$

where N_1 and N_2 are pore densities at area strains α_1 and α_2, respectively. We set $N_1=N_c(\alpha_1)$ such that at the critical condition ($\alpha=\alpha_1$), each RBC has exactly one pore. This condition is satisfied when $\alpha_1=0.16\%$, which also implies the existence of a minimum threshold strain below which no pores are created. The corresponding shear rate in steady shear is $G_f=3700\ s^{-1}$, calculated from Eq. 2. This assumption is supported by experimental observations[35] that pfHb does not increase when samples are sheared in the range $3000-3500\ s^{-1}$.

The value of N_2 comes from the membrane rupture condition. At the limit area strain $\alpha_2=6\%$ the relative pore area[32] is $A_P/A_m\approx 5.5\%$. At N_2, the first derivative of Eq. 6 must vanish to satisfy the minimum energy condition. Therefore

$$N_2=\frac{2Br_P-C}{4A{r_P}^3}=111\ \mu m^{-2}. \tag{10}$$

Here r_p is calculated from $A_P(\alpha_2)=\pi N_2 {r_P}^2 A_m(\alpha_2)=\pi A_m(\alpha_2)(2Br_P-C)/4Ar_P$. Combining Eq. 6 and 9 yields the total porated area on the membrane, for any value of α.

Transport of hemoglobin through the pores and expression of the Index of Hemolysis

The opening of pores initiates the release of intracellular content into plasma. Sublytic blood damage occurs when pores are large enough to allow Hb to escape ($r_{Hb}\approxeq 30$ nm). The Hb flux can be expressed in terms of the concentration difference between the cytoplasm and plasma

$$J_D=K_c(Hb_{RBC}\text{-}Hb_P)=K_c(Hb_B\text{-}Hb_P)Hct^{-1}, \tag{11}$$

where Hb_{RBC} is the intracellular Hb concentrations, Hct = 40% is the hematocrit, and K_c is the overall mass-transport coefficient.

Assuming homogeneous distribution of RBC size and shape, the mass balance for Hb_p in a batch of sheared blood is

$$\begin{aligned}\frac{dHb_p}{dt}&=\frac{K_c}{(1-Hct)}\frac{A_P(\alpha(t))}{V_{RBC}}\left[Hb_B\text{-}Hb_p(t)\right]\\&=R(\alpha(t),K_c)\left[Hb_B\text{-}Hb_p(t)\right].\end{aligned} \tag{12}$$

From Eqs. 1 and 12, the rate of hemolysis can be expressed as

$$\frac{dIH}{dt}=\frac{1}{Hb_B}\frac{dHb_p}{dt}=R(\alpha(t),K_c)\left(1-IH-\frac{Hb_p^0}{Hb_B}\right). \tag{13}$$

The term $R(\alpha(t),K_c)$ includes two contributions to the transport across RBC membrane (Figure 2): mass-transport rate, controlled by the overall mass-transfer coefficient K_c, and size of pores, dependent on area strain α.

For an initially undamaged blood sample, Eq. 13 can be integrated with the initial condition $IH(t=0)=0$, to obtain

$$IH(t)\approx 1-exp\left[-\int_0^t R(\alpha(t),K_c)\ dt\right]. \tag{14}$$

In physiological conditions $Hb_p^0/Hb_B\approx 10^{-4}\ll 1$; thus, this term is neglected in Eq. 14.

To estimate the mass-transfer coefficient K_c, the RBC is approximated as small, force-free particle in a shear dominated flow; hence, the rate of mass transport can be expressed as a function of the scalar fluid shear rate[36]

$$K_c=hG^k{}_f \tag{15}$$

Constants h and k were derived from fitting experimental data.

Results and Discussion

Figure 3 shows the results from the fitting of Eq. 15 against literature data of hemolysis in steady Couette flow.[37]

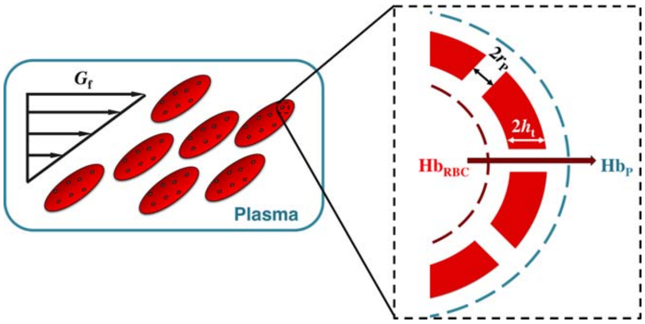

Figure 2. Model of hemoglobin transport in a control volume of blood subjected to fluid shear rate G_f.

Enlarged is the cross-sectional view of the RBC membrane of thickness containing circular pores of radius. A flux of hemoglobin is established, which is proportional to the overall mass-transport coefficient, and the concentration difference between the cytoplasm and the extracellular plasma (Hb_{RBC}-Hb_P). [Color figure can be viewed in the online issue, which is available at wileyonlinelibrary.com.]

The original data had to be corrected for two reasons. First, in the data, the hemolysis did not vanish in the absence of shearing, likely due to factors such as contact with exogenous surfaces.[38] Second the original definition of shear rate and exposure time did not account for the Poiseuille flow through the device. The analysis and correction procedure is reported in Supplementary Material.

Equation 15 was fit to experimental data at exposure time $t = 887$ ms, which is almost 10 times higher than the characteristic time of RBC deformation dictated by Eq. 2: $t_d=(f_2 G_f)^{-1}$. Therefore, at this exposure time range, the mass-transport rate can be assumed to depend only on the flow field around the cell as expressed by Eq. 15. The optimal fitted values of the constants are $h=1.67 \cdot 10^{-8}\mu\text{m s}^{(k-1)}$, $k=1.54$ (RMSE = $6.8 \cdot 10^{-3}$).

Figure 4 shows the comparison between other data sets from the same work[37] and predictions from MSBP model, at varying shear rate and for different values of exposure time. A satisfactory agreement was found for data sets in which $t \gg t_d$, whereas model predictions deviate from data when $t \approx t_d$. We suspect that such discrepancy might stem from an underestimation the membrane area strain at short exposure times. The parameters in the model of cell deformation (Eq. 2) were determined by considering cell rupture conditions, membrane relaxation time and restricting the parameter range so as to avoid cell shape oscillations in steady shear. This choice allows the model to predict RBC shape for higher shear rates and exposure times typical of cardiovascular devices, such as blood pumps and heart valves ($0.5 < t < 1$ s, $G_f > 20{,}000$ s^{-1}).[9]

To illustrate model predictions in complex flows and the integration with large-scale CFD computations, we chose a blood flow system with a curved pipe grafted to a straight channel. The Newtonian fluid velocity field was computed by the Galerkin/least-squares (GLS) finite element method with bilinear basis functions for both velocity and pressure,[39] using the third-order in space, second-order in time, in-house code XNS. Mesh and time-step size were chosen accordingly to a previously established methodology (details on flow governing equations, GLS formulation and flow solution strategy can be found authors' in previous works[40–42]). The choice of a Newtonian model for blood is commonly adopted when simulating high-shear flows (>100 s^{-1}). In such flow conditions that are typical of extracorporeal devices,[2] it has been shown[43] that the viscosity of human blood at 45% hematocrit and temperature of 37°C reaches a constant value of 3.5–4 mPa s. At lower shear rate, blood exhibits shear-thinning, viscoelastic and thixotropic properties, due to the shear-controlled aggregation and disaggregation of rouleaux and the Newtonian assumption cannot be considered valid. Extensive review of alternative constitutive equations for the description of properties at low shear rates can be found in Ref. 44. Blood flow in the domain Ω with boundary Γ was computed by solving the momentum and mass conservation equations for an incompressible fluid

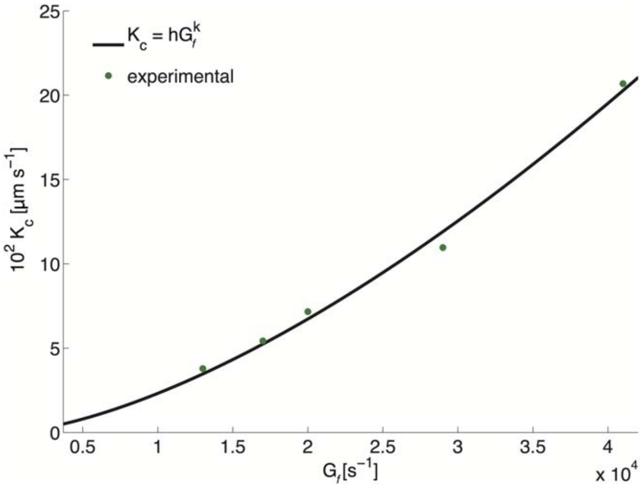

Figure 3. Overall mass-transport coefficient vs. shear rate.

Points represent the values calculated from experimental rate of hemolysis; the curve is the result of fitting hemolysis data from Heuser and Opitz[37] at $t = 887$ ms with Eq. 15. [Color figure can be viewed in the online issue, which is available at wileyonlinelibrary.com.]

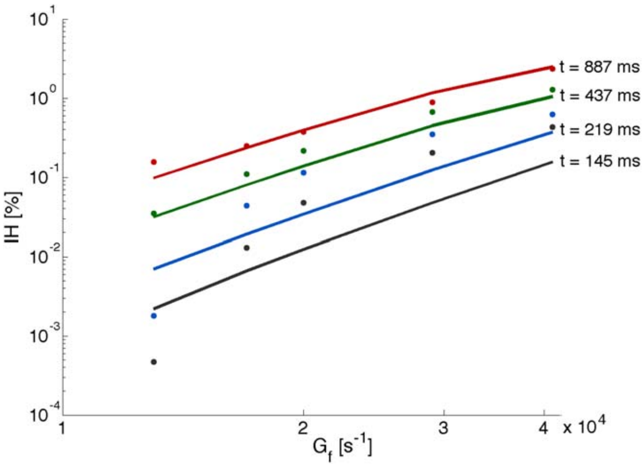

Figure 4. Index of hemolysis at four different exposure times.

Comparison between original Giersiepen data[10] (points) and model results (lines). Data set at $t = 887$ ms was used to fit K_c, whereas the other three data sets at $145 < t < 437$ ms were predicted with the model. [Color figure can be viewed in the online issue, which is available at wileyonlinelibrary.com.]

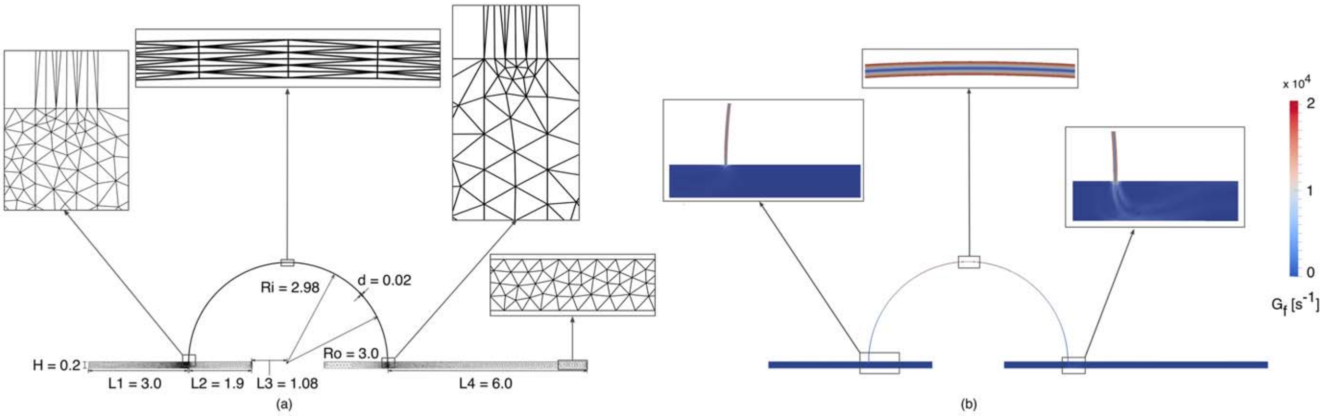

Figure 5. Flow in a curved pipe grafted to a straight channel (a) geometry (units in cm) and mesh, and (b) scalar shear rate profile.

[Color figure can be viewed in the online issue, which is available at wileyonlinelibrary.com.]

$$\rho\left(\frac{\partial \mathbf{u}}{\partial t}+\mathbf{u}\cdot\nabla\mathbf{u}\right)-\nabla\cdot\mathbf{T}=\mathbf{0} \tag{16}$$

$$\nabla\cdot\mathbf{u}=0 \tag{17}$$

where $\rho = 1056\ \text{kg m}^{-3}$ and $\mu = 3.5$ mPa s are blood density and viscosity, $\mathbf{u}$ is the velocity, $\mathbf{T}=p\mathbf{I}+\mu(\nabla\mathbf{u}+\nabla\mathbf{u}^{\mathrm{T}})$ is the total stress tensor, and p is the pressure. The computed velocity and pressure were used in Eq. 2 to calculate RBC deformation,[13] and the rate of hemolysis along 50 path lines equally spaced on the inlet section, starting at a distance of 150 μm from the upper wall boundary. Figure 5a shows the two-dimensional (2-D) flow domain. The inlet and outlet ports are $H = 0.2$ cm wide; the curved pipe radius is 200 μm. The Reynolds number is $\mathrm{Re} = \rho U_{\max} H/\mu$, where $U_{\max}$ is the maximum x-velocity at the inlet boundary. The fluid dynamic problem was solved at $\mathrm{Re} = 100$ by imposing no-slip ($\mathbf{u} = \mathbf{0}$) at the walls, and a fully developed parabolic velocity profile at the inlet ($\mathbf{u}(y) = \mathbf{i}U(y)$) and outlet ($\mathbf{n}\cdot\nabla\mathbf{u}=\mathbf{0}$, where $\mathbf{n}$ is the outward normal vector). The flow domain was discretized with an unstructured mesh of 8,124 triangular elements, refined near the inlet and outlet of the curved graft to trace particle path

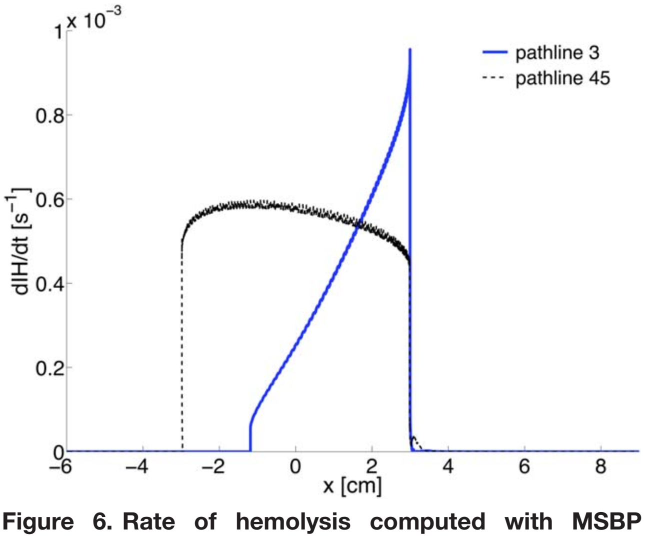

Figure 6. Rate of hemolysis computed with MSBP model on pathlines 3 and 45.

Inlet of the graft is at $x = -3$, outlet is at $x = 3$. [Color figure can be viewed in the online issue, which is available at wileyonlinelibrary.com.]

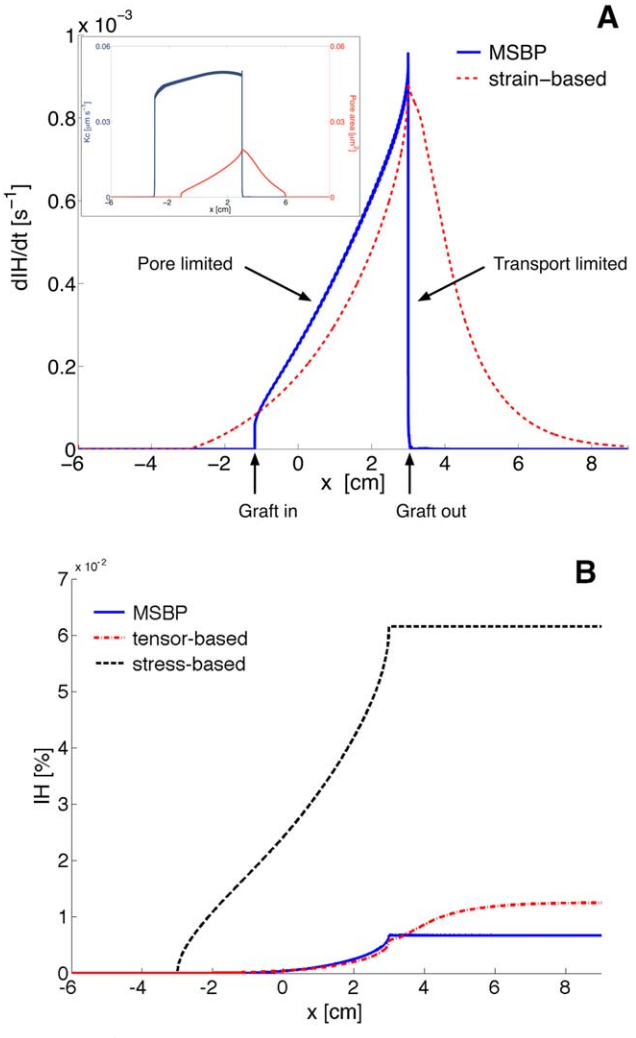

Figure 7. Comparison of results predicted by the different models on pathline 3 (A) rate of hemolysis. Inset: comparison between the overall mass-transport coefficient and pore area on pathline 3.

Inlet of the graft is at $x = -3$, outlet is at $x = 3$, and (B) index of hemolysis. [Color figure can be viewed in the online issue, which is available at wileyonlinelibrary.com.]

Table 3. Flow-Rate Averaged Index of Hemolysis, $\mathrm{IH_{avg}}$ [%]

	Stress-based	Strain-based	MSBP
Coefficients from eq. S10 in Supplementary Material	$3.340 \cdot 10^{-2}$	$1.623 \cdot 10^{-2}$	$6.532 \cdot 10^{-3}$
Coefficients from Giersiepen et al.[10]	$7.829 \cdot 10^{-2}$	$3.659 \cdot 10^{-2}$	

accurately (Figure 5a). Minor oscillations are caused by the interpolation of velocity $\mathbf{u}_n$ with piecewise linear functions. Figure 5b shows the fluid shear rate profile with a magnification of the zones upstream, downstream and center of the curved graft.

The advantages of the biophysical approach of the MSBP model can observed when the results for two particles initially subjected to same fluid shear rate are compared. Figure 6 shows the rate of hemolysis computed for the particles starting at a distance of 200 μm from the upper (pathline 3) and lower boundary (pathline 45), respectively. For the particle on pathline 3, no hemolysis occurs until the axial location $x = -1.2$, where the area strain reaches the threshold value and pores open on the membrane. Then the rate of hemolysis steeply increases inside the graft, following the RBC deformation and poration dynamics. On the other end, the particle on pathline 45 deforms almost instantaneously beyond the limit threshold for poration, due the shear pulse near the graft inlet. After this initial surge, the pore area and the rate of hemolysis remain almost constant inside the graft. At the exit of the curved pipe, the rate of hemolysis computed on both pathlines drops suddenly to $\approx 10^{-5}$ s^{-1}: this effect is due to the decrease of the rate of transport, which is controlled by the fluid shear rate G_f (Eq. 15). Thus, with this novel biophysical description it is possible to separate the factors controlling the hemolysis process: the pore opening mechanism provides an on-off switch for Hb flux and appears to be the rate-limiting step in the high-shear zones of flow domain. The convective mass-transport mechanism controls the intensity of the Hb flux at low shear rate even when RBCs are still relaxing from the deformed state (Figure 7a, inset). Such a description of the interplay between the flow dynamics conditions, the viscoelastic RBC deformation and permeabilization of the cell membrane and the transport of hemoglobin at the sublytic stage of hemolytic damage cannot be captured with current existing models. In Figure 7a the rate of hemolysis on pathline 3 computed with MSBP and tensor-based models are compared. In the tensor-based model the rate of hemolysis depends only on RBC deformation in all of the regions of the flow domain; the MSBP model allows to estimate the relative contribution of the causes of rate change. The total index of hemolysis along pathline 3 calculated with the stress-based, tensor-based and MSBP model is presented in Figure 7b. Stress-based[10] and tensor-based[11] models predict nonzero rate of hemolysis in the entire channel, even in the zones where the shear rate is well below the hemolytic thresholds[45] and, rather, close to values typical of physiological circulation[1] ($\sim$100–200 s^{-1}). Therefore, current models can lead to an overestimation of the index of hemolysis, particularly when stress-based models are used, due to the quadratic, instantaneous dependence of damage on the scalar shear stress.

The total average hemolysis index in the channel was computed using the flow-rate average of IH at the outlet of the graft ($\mathrm{IH_{avg}}$)

$$\mathrm{IH_{avg}} = \frac{\int_{\Gamma_0} \mathrm{IH}\,(\mathbf{u}\cdot\mathbf{n}_0)\,\mathrm{d}\Gamma}{\int_{\Gamma_0} (\mathbf{u}\cdot\mathbf{n}_0)\,\mathrm{d}\Gamma} \tag{18}$$

Equation 18 was used to compare blood damage predictions from MSBP model, stress-based model[10] and tensor-based model[11] (Table 3). Predictions of $\mathrm{IH_{avg}}$ with stress-based approach are 5–10 times higher than the other models, in agreement with findings of other studies.[46–49]

Conclusion

In this work, we describe a novel approach for estimation of hemolysis in complex blood flows, based on a multiscale, biophysical model. The model consists of three components: deformation and area strain of the cell, formation of membrane pores and transport of hemoglobin. The test of hemolysis prediction in model geometry shows that, through the inclusion on biophysical phenomena, the MSBP model enables the estimation of the multiple flow-induced processes that contribute to cell damage. The model can be integrated with CFD analysis for computational design and optimization of biomedical devices to potentially identify zones at higher hemolytic impact within the flow domain. Its predictive ability is presently limited by the lack of reliable and consistent in-vitro hemolysis measurements[38] taken at the short exposure times (< 500 ms) typical of VADs; such experimental data would permit the validation and tuning of the model in fast flows.

Each component of the MSBP model can be refined and improved independently. Ongoing work is directed toward the refinement of RBC deformation model, to include the membrane viscoelastic response to short time shearing and toward enhancing the mass-transfer model.

Acknowledgments

This work was supported by Grant No. R01HL085054 awarded to Texas Heart Institute (THI) by the National Heart, Lung, and Blood Institute (NHLBI) and by the National Science Foundation of the USA under grant DMS-0811160. The content is solely the responsibility of the authors and does not necessarily represent the official views of NHLBI or the National Institutes of Health. The authors are grateful to Dr. Joel Moake for the helpful discussions and suggestions during the manuscript preparation.

Conflict of Interest Statement

The authors declare no conflict of interest associated with this work.

Literature Cited

1. Ku DN. Blood flow in arteries. *Annu Rev Fluid Mech.* 1997;29:399–434.
2. Tillmann W, Reul H, Herold M, Bruss KH, van Gilse J. In-vitro wall shear measurements at aortic valve prostheses. *J Biomech.* 1984;17:263–279.
3. Kameneva MV, Antaki JF, Borovetz, HS, Griffith BP, Butler KC, Yeleswarapu KK, Watach MJ, Kormos RL. Mechanisms of red blood cell trauma in assisted circulation: rheologic similarities of red blood cell transformations due to natural aging and mechanical stress. *ASAIO J.* 1995;41:M457–60.
4. Blackshear PL, Blackshear GL. Mechanical Hemolysis. In: Skalak R, Chien S. *Handbook of Bioengineering*. New York: McGraw-Hill;1987:15.1–19.

5. Girdhar G, Bluestein D. Biological effects of dynamic shear stress in cardiovascular pathologies and devices. *Expert Rev Med Devices.* 2008;5:167–181.
6. De Wachter DS, Verdonck PR, De Vos JY, Hombrouckx RO. Blood trauma in plastic haemodialysis cannulae. *Int J Artificial Organs.* 1997;20:366–370.
7. Sharp MK, Mohammad SF. Scaling of hemolysis in needles and catheters. *Annals Biomed Eng.* 1998;26:788–797.
8. Leverett LB, Hellums JD, Alfrey CP, Lynch EC. Red blood cell damage by shear stress. *Biophys J.* 1972;12:257–273.
9. Zhang T, Taskin ME, Fang HB, Pampori A, Jarvik R, Griffith BP, Wu ZJ. Study of flow-induced hemolysis using novel couette-type blood-shearing devices. *Artificial Organs.* 2011;35:1180–1185.
10. Giersiepen M, Wurzinger LJ, Opitz R, Reul H. Estimation of shear stress-related blood damage in heart valve prostheses–*in vitro* comparison of 25 aortic valves. *Int J Artificial Organs.* 1990;13: 300–306.
11. Arora D, Behr M, Pasquali M. A tensor-based measure for estimating blood damage. *Artificial Organs.* 2004;28:1002–1015.
12. Chen Y, Kent TL, Sharp MK. Testing of models of flow-induced hemolysis in blood flow through hypodermic needles. *Artificial Organs.* 2013;37:256–266.
13. Arora D, Behr M, Pasquali M. Hemolysis estimation in a centrifugal blood pump using a tensor-based measure. *Artificial Organs.* 2006; 30:539–547.
14. Evans E A, Waugh R, Melnik L. Elastic area compressibility modulus of red cell membrane. *Biophys J.* 1976;16:585–595.
15. Rand RP. Mechanical properties of the red cell membrane II. *Viscoelastic breakdown of the membrane. Biophys J.* 1964;4:303–316.
16. Linderkamp O, Meiselman HJ. Geometric, osmotic, and membrane mechanical properties of density-separated human red cells. *Blood.* 1982;59:1121–1127.
17. Guido S, Tomaiuolo G. Microconfined flow behavior of red blood cells *in vitro*. *Comptes Rend. Phys.* 2009;10:751–763.
18. Chang DC, Reese TS. Changes in membrane structure induced by electroporation as revealed by rapid-freezing electron microscopy. *Biophys J.* 1990;58:1–12.
19. Hallow DM, Seeger RA, Kamaev PP, Prado GR, LaPlaca MC, Prausnitz MR. Shear-induced intracellular loading of cells with molecules by controlled microfluidics. *Biotechnol Bioeng*. 2008;99:846–854.
20. Ohta Y, Okamoto H, Kanno M, Okuda T. Atomic force microscopic observation of mechanically traumatized erythrocytes. *Artificial Organs.* 2002;26:10–17.
21. Henon S, Lenormand G, Richert A, Gallet F. A new determination of the shear modulus of the human erythrocyte membrane using optical tweezers. *Biophys J.* 1999;76:1145–1151.
22. Schmid-Schonbein H, Gaehtgens P, Hirsch H. On the shear rate dependence of red cell aggregation *in vitro*. *J Clin Invest.* 1968;47: 1447–1454.
23. Korin N, Bransky A, Dinnar U. Theoretical model and experimental study of red blood cell (RBC) deformation in microchannels. *J Biomech.* 2007;40:2088–2095.
24. Schmid-Schonbein H, Wells R. Fluid drop-like transition of erythrocytes under shear. *Science.* 1969;165:288–291.
25. Down LA, Papavassiliou DV, O'Rear EA. Significance of extensional stresses to red blood cell lysis in a shearing flow. *Annals Biomed Eng.* 2011;39:1632–1642.
26. Maffettone PL, Minale M. Equation of change for ellipsoidal drops in viscous flow. *J Non-Newton Fluid.* 1998;78:227–241.
27. Arora D. A Tensor-based Measure for Estimating Blood Damage (vol 28, pg 1002, 2004). *Artif Organs.* 2012;36:500.
28. Keller SR, Skalak R. Motion of a tank-treading ellipsoidal particle in a shear flow. *J Fluid Mech.* 1982;120:27–47.
29. Israelachvili JN. *Intermolecular and Surface Forces.* 2nd ed. London, UK: Academic Press;1992.
30. Neu JC, Krassowska W. Modeling postshock evolution of large electropores. *Phys Rev E Stat Nonlin Soft Matter Phys.* 2003;67:021915.
31. Litster JD. Stability of lipid bilayers and red blood cell membranes. *Physics Lett A.* 1975;53:193–194.
32. Fournier L, Joos B. Lattice model for the kinetics of rupture of fluid bilayer membranes. *Phys Rev E Stat Nonlin Soft Matter Phys.* 2003; 67:051908.
33. DeBruin KA, Krassowska W. Electroporation and shock-induced transmembrane potential in a cardiac fiber during defibrillation strength shocks. *Annals Biomed Eng.* 1998;26:584–596.
34. Needham D, Hochmuth RM. Electro-mechanical permeabilization of lipid vesicles. *Role of membrane tension and compressibility. Biophys J.* 1989;55:1001–1009.
35. Garvey CJ, Knott RB, Drabarek E, Kuchel PW. Shear-induced alignment of self-associated hemoglobin in human erythrocytes: small angle neutron scattering studies. *Eur Biophys J.* 2004;33:589–595.
36. Frankel NA, Acrivos A. Heat and mass transfer from small spheres and cylinders freely suspended in shear flow. *Phys Fluids.* 1968;11: 1913–1918.
37. Heuser G, Opitz R. A Couette viscometer for short time shearing of blood. *Biorheology.* 1980;17:17–24.
38. Mueller MR, Schima H, Engelhardt H, Salat A, Olsen DB, Losert U, Wolner E. *In vitro* hematological testing of rotary blood pumps: remarks on standardization and data interpretation. *Artificial Organs.* 1993;17:103–110.
39. Behbahani M, Behr M, Hormes M, Steinseifer U, Arora D, Coronado O, Pasquali M. A review of computational fluid dynamics analysis of blood pumps. *Eur J Appl Math.* 2009;20:363–397.
40. Behr M, Tezduyar TE. Finite element solution strategies for large-scale flow simulations. *Comp Meth Appl M.* 1994;112:3–24.
41. Behr M, Arora D. Shear-slip mesh update method: implementation and applications. *Comput Methods Biomech Biomed Eng.* 2003;6: 113–123.
42. Behr M, Arora D, Nose Y, Motomura, T. Performance analysis of ventricular assist devices using finite element flow simulation. *Int J Numer Meth Fl.* 2004;46:1201–1210.
43. Chien S. Shear dependence of effective cell volume as a determinant of blood viscosity. *Science.* 1970;168:977–979.
44. Robertson AM, Sequeira A, Owens RG. Rheological models for blood. In: Formaggia L, Quarteroni A, Veneziani A. *Cardiovascular Mathematics*. New York: Springer; 2009:211–41.
45. Chen Y, Sharp MK. A strain-based flow-induced hemolysis prediction model calibrated by *in vitro* erythrocyte deformation measurements. *Artificial Organs.* 2011;35:145–156.
46. Goubergrits L, Affeld K. Numerical estimation of blood damage in artificial organs. *Artificial Organs.* 2004;28:499–507.
47. Paul R, Apel J, Klaus S, Schugner F, Schwindke P, Reul H. Shear stress related blood damage in laminar couette flow. *Artificial Organs.* 2003;27:517–529.
48. Pauli L, Nam J, Pasquali M, Behr M. Transient stress-based and strain-based hemolysis estimation in a simplified blood pump. *Int J Numer Method Biomed Eng.* 2013;29:1148–1160.
49. de Tullio, MD, Nam J, Pascazio G, Balaras E, Verzicco R. Computational prediction of mechanical hemolysis in aortic valve prostheses. *Eur J Mech B-Fluid.* 2012;35:47–53.

Manuscript received Sept. 5, 2013, and revision received Nov. 15, 2013.